Structural characterization of cerium-doped hydroxyapatite nanoparticles synthesized by an ultrasonic-assisted sol-gel technique

Piaw Phatai[a,b,*], Cybelle Morales Futalan[c], Songkot Utara[a,b], Pongtanawat Khemthong[d], Sirilak Kamonwannasit[e]

[a] Department of Chemistry, Faculty of Science, Udon Thani Rajabhat University, Udon Thani 41000, Thailand
[b] Polymer and Material Research Group, Faculty of Science, Udon Thani Rajabhat University, Udon Thani 41000, Thailand
[c] National Research Center for Disaster-Free and Safe Ocean City, Busan 49315, Republic of Korea
[d] NANOTEC, National Science and Technology Development Agency (NSTDA), 111 Thailand Science Park, Thanon Phahonyothin, Tambon Khlong Nueng, Amphoe Khlong Luang, Pathum Thani 12120, Thailand
[e] Department of Natural Product Technology, Faculty of Agricultural Technology, Burapha University, Sakaeo Campus, Sakaeo 27160, Thailand

ARTICLE INFO

ABSTRACT

This present work focuses on the synthesis of cerium-doped hydroxyapatite (Ce/HAp-US) using an ultrasonic-assisted sol-gel technique under varying concentration of Ce from 0.5% to 2.0%. The preparative method utilized the stoichiometric molar ratio of Ca to P of 1.67 where the Ce/HAp samples were calcined at 600 °C for 2 h. The structural properties of Ce/HAp samples were characterized by various techniques including X-ray absorption near edge spectroscopy (XANES), X-ray powder diffraction (XRD), Fourier transform infrared spectroscopy (FT-IR), transmission electron microscopy (TEM) and energy dispersive X-ray spectroscopy (EDX). Results from the XANES spectra of xCe/HAp samples at the Ce L_3-edge reveal that the dominant species of cerium was Ce^{4+} along with some Ce^{3+}, which have been incorporated into the HAp lattice. Results of the EDX analysis show that the Ca/P molar ratio of xCe/HAp decreased with an increase in Ce content. XRD analysis confirms that Ce^{3+} and Ce^{4+} were partially incorporated into the hexagonal framework of HAp and rhombohedral structure of β-tricalcium phosphate (β-TCP). FT-IR measurements identified the main functional groups of Ce/HAp to be hydroxyl (OH^-), phosphate (PO_4^{3-}) and carbonate (CO_3^{2-}). The morphology obtained from TEM analysis illustrates that pure HAp-US is composed of very fine spherical particles. By incorporating Ce ions into the HAp lattice, the presence of dense dark spots, possibly the loaded Ce species, were observed.

Introduction

Synthetic hydroxyapatite (HAp), with chemical formula of $Ca_{10}(PO_4)_6(OH)_2$, is considered to be an essential macroporous inorganic element found in human hard tissues that include dentine, enamel, and bones [1]. In addition, it has a very similar crystallographic and chemical structure with the bone mineral that is typically composed of 25–75% HAp by weight with a calcium-to-phosphate stoichiometric ratio of 1.67 [2–3]. In general, the inorganic portion of bones are composed of crystalline HAp nanoparticles that are 20–30 nm in width, 100 nm in length and 3–6 nm in thickness while enamel of the teeth contains 95% HAp that are submicron in size [4]. HAp materials are characterized by several excellent properties such as bioactivity, osseointegrity, non-toxicity, biocompatibility, osteoinduction, osteoconductivity, high affinity for pathogenic microbes, satisfactory ion

exchange capability with heavy metals, selective adsorption of proteins and organic compounds, and capacity to directly interact and form chemical bonds with human hard tissues [5–9]. Thus, there is a wide application of HAp in the biomedical field such as dentistry [10], maxillofacial reconstruction [11], craniofacial augmentation [12], tissue scaffolding materials [13], ossicular chain reconstruction in otolaryngological surgery [14], and coating of metallic implants [15]. Moreover, HAp is also utilized in non-medical applications such as chemical sensors in liquid chromatography columns [16], catalysts [17], gas sensors [17], drug delivery system [18] and adsorbent in wastewater treatment [19]. However, pure HAp polycrystals in its bulk form, display poor bending strength, brittleness, reduced fatigue resistance and low toughness [20], which prevents its utilization in mechanical load bearing applications. Other limitations of pure HAp include slow dissolution rate [21], chemically weak properties in acidic

* Corresponding author at: Department of Chemistry, Faculty of Science, Udon Thani Rajabhat University, Udon Thani 41000, Thailand.
E-mail address: piawtee99@hotmail.com (P. Phatai).

systems [22] and low antibacterial capacity [23].

Recently, the development of nano-sized HAp has attracted attention due to improved functional properties such as smaller grain size, large surface area, better mechanical strength, enhanced surface reactivity, bioactivity and osteoblast cell adhesion [24–25]. Most importantly, these characteristics are favorable for implant-cell interaction *in vivo* [26]. Another method that would help overcome the disadvantages of pure HAp is through substitution of Ca^{2+} ion with various metal ions such as Ag^+, Al^{3+}, K^+, Ce^{3+}, Mg^{2+}, Zn^{2+}, La^{3+}, Sr^{2+}, Y^{3+} and In^{3+} [27–29]. Ionic substitutions affect the crystallinity, lattice parameters, composition and morphology of HAp materials that would lead to the improvement of properties such as chemical and mechanical stability, cytocompatibility, solubility, bioactivity and antibacterial property [30–34].

Cerium (Ce) is characterized with its partially filled electron orbital at 4f and 5d subshells. Depending on the chemical environment, Ce could attain valence states at $+3$ and $+4$ after it has undergone excitation [35]. Ce can act in a manner similar to calcium (Ca^{2+}), wherein it accumulates in bones in small amount and stimulates metabolic activity in organisms [36,37]. The Ce ion exists in two forms, Ce^{3+} and Ce^{4+} where its unique ability to switch between oxidation states could cause the redox-active cerium nanoceria (CeO_2) to exhibit antibacterial and antioxidant activities [38]. The reduction of CeO_2 from Ce^{4+} to Ce^{3+} occurs due to the creation of oxygen vacancies without changing its structure. Moreover, there is a wide application of Ce in medicine such as catheters, healing of burn wounds and dentistry [27,39,40]. Previous studies synthesized Ce-doped HAp using hydrothermal technique [41,42], Ce^{4+} doped HAp via sol-gel method [23,38,43] and coprecipitation method [16], Sr/Ce-doped HAp via microwave irradiation method [44], Ce-doped HAp/polylactic acid coating via chemical precipitation method [45] and Au/Ga-doped HAp through ultrasonic-assisted precipitation method [46].

Among the numerous techniques, the sol-gel method has been widely utilized in the synthesis of HAp nanoparticles due to its cost-effectivity, ease of handling and application to complex shapes during coating, requirement of lower sintering temperature, desired surface morphology, simple to set-up and precursor mixing occurs at the molecular level that would result to excellent homogenous HAp particles [47–49]. In addition, HAp particles prepared by the sol-gel method are characterized by high purity and crystallinity and occurrence of less agglomeration where the proper stoichiometry between Ca and P is easily attainable [50–52].

Numerous industrial activities have employed the ultrasonic-assisted method for the synthesis of nanomaterials. Ultrasound utilizes acoustic cavitation effect in a medium that would result in enhanced dissolution of reagents and improved rate of reaction between solid and liquid reactants [53–55]. Moreover, ultrasound lowers the induction period of crystallization, which refers to the time of formation and growth of the critical nucleus [56]. Other advantages of ultrasound include formation of nano-sized HAp particles that are uniform and spherical in shape with a high crystalline fraction, high specific area and minimal agglomeration [55]. Varadarajan et al. (2014) observed that ultrasonication of calcium-deficient HAp can increase the degree of nano-crystallinity characterized by its increased crystal aspect ratio and needle-like morphology [25]. Kurtjak et al. (2017) concluded that ultrasonic-assisted precipitation method could provide good distribution of nanogold and gallium-doped HAp [46].

In this study, the effect of varying Ce loading (range of molar fractions: 0, 0.5, 1.0, 1.5, 2.0) on xCe/HAp nanoparticles prepared using an ultrasonic-assisted sol-gel technique was investigated. The synthesized HAp nanoparticles were characterized using X-ray absorption near edge spectroscopy (XANES), X-ray powder diffraction (XRD), Fourier transform infrared spectroscopy (FT-IR), transmission electron microscopy (TEM) and energy dispersive X-ray spectroscopy (EDX). Thus, the effect on the structural properties when Ce^{3+} and Ce^{4+} ions are incorporated into HAp was evaluated. Results would yield crucial

information for further studies in the biomedical applications of Ce-containing HAp synthesized using the ultrasonic-assisted sol-gel method.

Materials and methods

Materials

All chemical reagents were of analytical grade and utilized without further purification. Calcium nitrate tetrahydrate ($Ca(NO_3)_2 \cdot 4H_2O$, 99.9 wt%), di-ammonium hydrogen phosphate (($NH_4)_2HPO_4$, 99.0 wt %), and ethanol (C_2H_5OH, 99.7–100%) were procured from QREC while cerium nitrate hexahydrate ($Ce(NO_3)_3 \cdot 6H_2O$, 99.0 wt%) was purchased from Acros.

Synthesis of HAp and xCe/HAp

The HAp nano-particles with the chemical formula, $Ca_{1-x}Ce_x(PO_4)_6(OH)_2$, denoted as xCe/HAp were synthesized by using a sonochemical method similar to that of Utara et al. [57]. There was no adjustment of pH made throughout the synthesis of HAp. A pre-determined mass of $Ca(NO_3)_2 \cdot 4H_2O$ dissolved in 100 mL of C_2H_5OH and ($NH_4)HPO_4$ dissolved in 25 mL of DI water are poured into a 500 mL beaker, where the mixture is magnetically stirred at 25 °C for 30 min. Then, $Ce(NO_3)_3 \cdot 6H_2O$ in 25 mL of DI water was slowly added into the mixture in a drop-wise method and stirred continuously for 30 min. Then, the mixture was transferred into a 100 mL Schlenk flask (diameter 5.0 cm) and was irradiated using the following conditions: frequency of 25 kHz, ultrasonication time of 30 min, and temperature of 25 ± 1 °C. The reactor was controlled using a thermocouple probe (Agilent U1185A; J-Type). The mixture was continuously stirred using a hotplate at 100 °C until dry. Finally, calcination was carried out by heating the dried samples to 600 °C at 3 °C/min where temperature of 600 °C was maintained for 2 h, which would yield the synthesized HAp powder. Various compositions of xCe/HAp (x = 0, 0.5, 1.0, 1.5 and 2.0) without ultrasonic irradiation are denoted as HAp-nUS, 1.0Ce/HAp-nUS, 2.0Ce/HAp-nUS while samples synthesized with ultrasonic irradiation are represented as HAp-US, 0.5Ce/HAp-US, 1.0Ce/HAp-US, 1.5Ce/HAp-US and 2.0Ce/HAp-US.

Characterization techniques

The spectra and valence state of Ce were analyzed using Ce L_3-edge XANES in the fluorescent mode at 25 °C using the beamline 5.2 of the Synchrotron Light Research Institute (Thailand). Each Ce/HAp-US sample was pressed into a frame covered by polyimide tape and mounted onto a sample holder. The normalization of the XANES spectra such as data fitting and background correction was carried out using the ATHENA program and compared to the reference materials such as Ce $(NO_3)_3 \cdot 6H_2O$ and CeO_2 as Ce^{3+} and Ce^{4+}, respectively. The crystal phase identification and purity of HAp and xCe/HAp were evaluated using an XRD (D8 Advance Series 2, Bruker, Germany) with an accelerating voltage of 40 kV, current of 35 mA, range of 2θ from 20° to 60° and Cu Kα radiation ($\lambda = 1.54184$ Å). The functional group of the prepared samples was determined using a FT-IR spectroscope (Spectrum two-Perkin Elmer) in the range of 500–4000 cm^{-1}. The shape, particle size, and distribution of HAp particles were measured by TEM (JEM-2100 Jeol) with an accelerating voltage of 200 kV where samples were dispersed in methanol, sonicated for 10 min in order for the uniform distribution of the particles in the solution. Elemental analysis of the weight and atomic percentages of Ca, P, O, and Ce and Ca/P ratio were determined using EDX analysis (S-3000 N HITACHI).
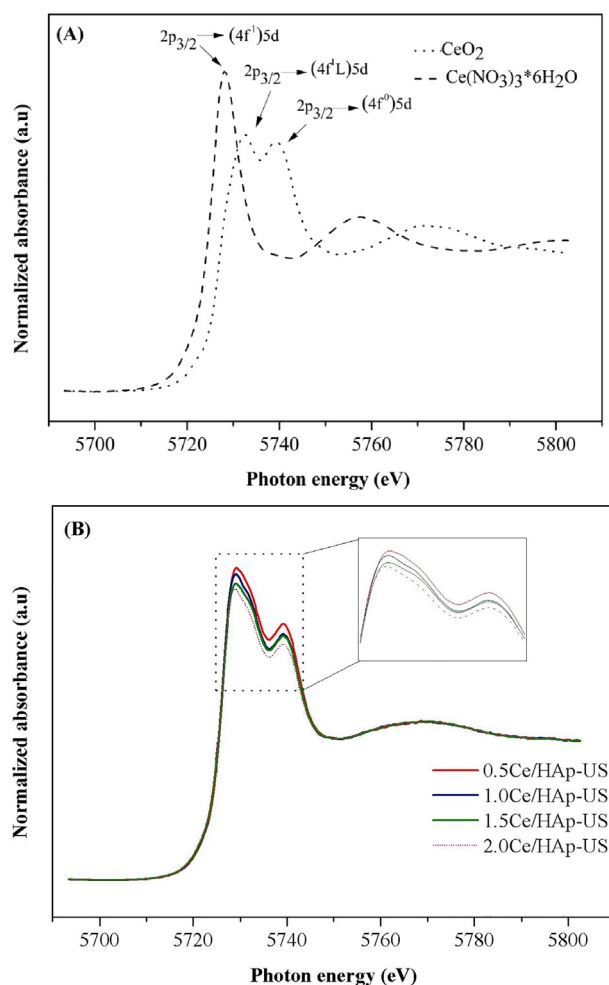
Fig. 1. Normalized XANES spectra of (A) reference standard materials (B) Ce/HAp-US samples.

Results and discussion

XANES analysis

To determine the valence state of the Ce species in the HAp structure, the Ce L$_3$–edge XANES spectra were investigated. Fig. 1A shows the characteristic of XANES fingerprint for Ce(NO$_3$)$_3$·6H$_2$O and CeO$_2$. In the white line peak of Ce(NO$_3$)$_3$·6H$_2$O, a single absorption maxima at 5728.31 eV is observed that refers to the electronic transition of $2p_{3/2} \rightarrow (4f^1)$ 5d. On the other hand, the CeO$_2$ spectrum are comprised of two peaks that are located at 5732.52 and 5739.24 eV, which are attributed to the $2p_{3/2} \rightarrow (4f^1L)$ 5d and $2p_{3/2} \rightarrow (4f^0)$ 5d transitions, respectively. The "L" indicates that an electron in the 2p orbital of oxygen was transferred to the 4f orbital of a Ce atom [58] and the energy difference between the two peaks is about 7 eV, which is similar to that reported in the literature [59]. In Fig. 1B, the XANES spectra of Ce/HAp-US samples showed two peaks confirming that the valence state of Ce varied between +4 and +3, which depended mostly on the degree of oxygen deficiency. Based from the inset of the peaks, it can be observed that the intensity of the spectra of Ce/HAp-US samples slightly decreased as the Ce loading was increased from 0.5 to 2.0% that could be attributed to the concentration effect.

To identify the changes in the Ce oxidation state, a quantitative analysis was carried out by curve-fitting the XANES spectra using multi-peak Gaussian functions that was applied to the peak features [59,60]. Fig. 2 shows the deconvolution result of Ce L$_3$-edge XANES spectra of the 0.5Ce/HAp-US sample. It could be observed that there is the
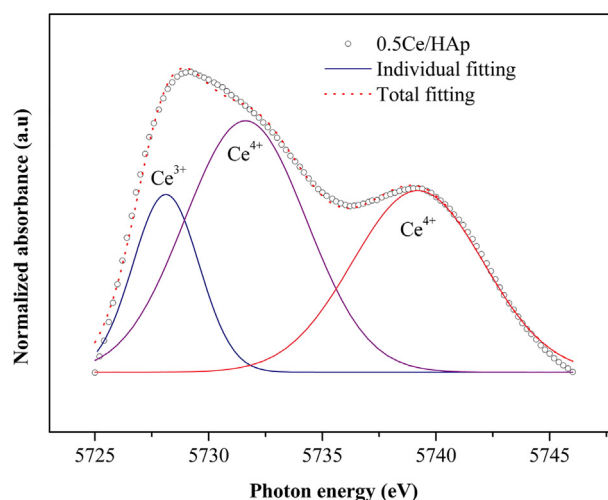

Fig. 2. Curve-fitting of Ce L$_3$ XANES spectra of 0.5Ce/HAp-US sample with multi-peak Gaussian functions.

coexistence of Ce^{3+} and Ce^{4+} states (as a Ce^{4+}/Ce^{3+} redox couple). The valence state of Ce^{4+} was determined to be the dominant form on the surface of Ce-substituted HAp samples where Ce^{3+} readily undergoes oxidation to form Ce^{4+} in the presence of oxygen during calcination. The fractions of Ce^{3+} and Ce^{4+} states in the samples were computed using Eqs. (1) and (2):

$$[Ce^{3+}] = A(Ce^{3+})/[A(Ce^{3+}) + A(Ce^{4+})] \tag{1}$$

$$[Ce^{4+}] = A(Ce^{4+})/[A(Ce^{3+}) + A(Ce^{4+})] \tag{2}$$

where A(Ce^{3+}) and A(Ce^{4+}) are the total integrated peak areas corresponding to the Ce^{3+} and Ce^{4+} XANES signals, respectively [59].

Results indicate that all the Ce-substituted HAp-US samples contain about 17–18% of Ce^{3+} where there is no significant difference observed in the Ce^{3+} content under varying Ce loading (Table 1). The occurrence of Ce^{3+} in HAp samples could be attributed to the thermal reduction of Ce^{4+} to Ce^{3+} during high calcination temperature (600 °C). The conversion of Ce^{4+} into Ce^{3+} could be due to the electron acceptance of Ce^{4+} from an adjacent oxygen anion such as PO$_4$$^{3-}$ or some other electron contributor [61–62]. Moreover, conversion to Ce^{3+} is attributed to the presence of an oxygen defect or oxygen vacancy at the surface [63]. Similar results were obtained by Li et al. (2015) where an increase of calcination temperature in air from 400 to 600 °C caused a gradual increase in the ratio of Ce^{3+}/Ce^{4+}. It can be inferred that the calcination temperature at 600 °C played a vital role in the transformation of Ce^{4+} to Ce^{3+}, which has a positive effect on the catalytic performance over a wide temperature range [64].

Table 1

Lattice parameters of xCe/HAp samples obtained from XRD analysis and percentage of Ce^{3+} obtained from XANES analysis.

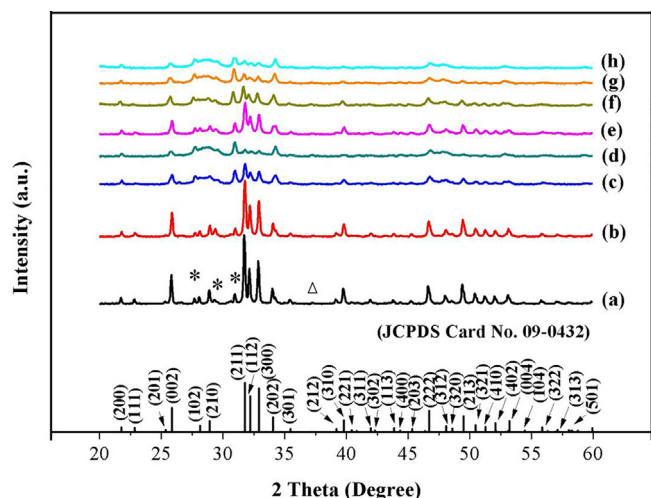| Samples	Lattice parameters (nm)		Ce^{3+} (%)	D (nm)
	a	c		
HAp-nUS	0.9447 ± 0.0036	0.6895 ± 0.0006	–	63.7
HAp-US	0.9412 ± 0.0024	0.6884 ± 0.0001	–	51.6
1.0Ce/HAp-nUS	0.9435 ± 0.0075	0.6901 ± 0.0031	–	52.9
2.0Ce/HAp-nUS	0.9442 ± 0.0105	0.6926 ± 0.0004	–	63.7
0.5Ce/HAp-US	0.9451 ± 0.0042	0.6879 ± 0.0004	17.81	52.9
1.0Ce/HAp-US	0.9427 ± 0.0065	0.6913 ± 0.0022	18.21	52.9
1.5Ce/HAp-US	0.9438 ± 0.0137	0.6925 ± 0.0005	17.75	45.5
2.0Ce/HAp-US	0.9432 ± 0.0239	0.6929 ± 0.0002	18.33	63.7

Fig. 3. XRD patterns of samples: (a) HAp-nUS, (b) HAp-US (c) 1.0Ce/HAp-nUS (d) 2.0Ce/HAp-nUS, (e) 0.5Ce/HAp-US, (f) 1.0Ce/HAp-US, (g) 1.5Ce/HAp-US and (h) 2.0Ce/HAp-US. [* β-TCP, Δ CaO].

Powder XRD analysis

Fig. 3 illustrates the phase composition and lattice parameter of HAp and xCe/HAp (under various concentration of Ce) after calcination at 600 °C for 2 h. All xCe/HAp samples exhibited the typical hexagonal crystalline behavior of HAp (space group $P6_3/m$) with corresponding peaks of 2θ at 25.8° (0 0 2), 31.8° (2 1 1), 32.9° (1 1 2), 34.1° (2 0 2), 39.8° (3 1 0), 46.7° (2 2 2) and 49.5° (2 1 3) (JCPDS No. 09-0432).

In general, the spectra collected from the Ce/HAp samples are similar to those obtained from pure HAp sample. However, the addition of Ce into HAp structure causes the peaks to shift and slightly broaden. Moreover, the relative intensity of all diffraction peaks was observed to slightly decrease with increasing amount of Ce in HAp. This implies a decrease in crystallinity with increasing Ce content, which could be due to a different charge compensation mechanism during the substitution of Ca^{2+} by Ce^{3+} or Ce^{4+} [60]. In addition, this indicates that the Ce/ HAp samples are not simple composites of individual HAp and Ce oxides. Rather, it takes the form of a HAp solid solution with Ce^{3+} or Ce^{4+} embedded in its crystal structure. The ease of substitution of Ce^{3+} or Ce^{4+} with Ca^{2+} in the lattice could be attributed to the ionic radii of Ce^{3+} (0.114 nm) and Ce^{4+} (0.097 nm), which are comparable to that of Ca^{2+} (0.106 nm) [61,63]. In all xCe/HAp samples, the formation of secondary phases such as β-tricalcium phosphate (β-TCP, $Ca_3(PO_4)_2$) were observed, which could be correlated to the peaks at 2θ = 27.6°, 29.4° and 31.0° (JCPDS No. 09-0169). In addition, calcium oxide (CaO) was detected at 2θ = 38.2° (JCPDS No. 09-0169).

In a general hexagonal crystal system, the relationship between the crystal plane index and interplanar distance (d_{hkl}) is given by Eq. (3) [65]:

$$\frac{1}{d_{hkl}} = \left[\frac{4(h^2 + k^2 + hk)}{3a^2} + \left(\frac{l^2}{c^2} \right) \right]^{1/2}$$

(3)

where h, k and l are the miller indices of the crystal plane, and a and c are the lattice parameters. Based on Table 1, the values of "a" and "c" of the as-synthesized HAp-nUS and HAp-US are close to those of stoichiometric HAp (JCPDS Card No. 09-0432; $a = 0.9418$ nm and $c = 0.6884$ nm). When Ce^{3+} and Ce^{4+} were partially incorporated into HAp, the a and c values slightly increased due to the marginal distortion caused by the substitution of Ce^{3+} and Ce^{4+} in the crystal lattice structure of HAp [66]. Results confirm that cerium ions (Ce^{3+}/ Ce^{4+}) were partially incorporated into the HAp lattice during synthesis.

The average crystallite size D (nm) of the sample is calculated using the Scherrer equation:

$$D = \frac{k\lambda}{\beta \cos \theta}$$

(4)

where λ is the wavelength of Cu Kα radiation ($\lambda = 0.15418$ nm), β is the full width at half maximum intensity value for the diffraction peak under consideration (radian), θ is the diffraction angle of the corresponding reflection (°), and k is the broadening constant varying with crystal habit. For the quantitative determination, the peak at (0 0 2) was selected in the calculation of the crystallite size of HAp powders due to its adequate resolution and absence of interferences. As shown in Table 1, it can be observed that the crystallite size of HAp-nUS (63.7 nm) is higher than HAp-US (51.6 nm). In general, effect of ultrasonic irradiation leads to the lower crystallite size with the exception of 2.0Ce/HAp-US, which displayed the largest crystallite size.

Regarding the substitution mechanism, the lattice of the HAp generally contains two Ca atoms with different crystal configurations denoted as Ca(1) and Ca(2). The Ca(1) atoms occupy the columnar sites and are nine-fold coordinated. The Ca(2) atoms are located in the channels that pass through the 3D network of the PO_4^{3-} tetrahedra that are coordinated seven-fold [61]. The effective ionic radii of Ca^{2+} for Ca (1) and Ca(2) are 0.118 and 0.106 nm, respectively. Moreover, the radius of Ce^{3+} and Ce^{4+} is 0.107 and 0.097 nm, respectively [62]. Previous reports have shown that foreign ions with larger radius and smaller charge preferentially occupies the Ca(1) site while compact Ca (2) would be substituted with foreign ions that have smaller radius and greater charge [67,68]. In the present study, the difference in size of ionic radii suggests that Ce^{4+} should predominantly favor substitution in the Ca(2) site while Ca(1) site would be occupied preferentially by Ce^{3+} since it has a larger ionic radii than Ce^{4+}.

FT-IR analysis

In Fig. 4(a–b), the FT-IR spectra of HAp-nUS and HAp-US samples are represented by the following peaks: 3575 and 638 cm^{-1} refer to the stretching and bending of -OH group, 609 and 570 cm^{-1} represent the bending mode of the phosphate (O-P-O) group, and 1099 and 1038 cm^{-1} refer to the asymmetrical and symmetrical stretching modes of P-O and PO_4^{3-} [69–71]. The weak absorption bands at 3575 and 638 cm^{-1} in pure HAp indicate the existence of physisorbed water molecules.

As shown in Fig. 4(c–h), the -OH bands at 3575 cm^{-1} were observed to weaken within the range from 3474 to 3486 cm^{-1}. This is due to the disturbance in the electrical balance in HAp caused by the substitution of Ce^{3+}/ Ce^{4+} for Ca^{2+}, where some of the -OH were converted into O^{2-} in order to balance the charges [72]. The peaks located around 1302–1512 cm^{-1} are due to the stretching vibration of C-O of carbonate (CO_3^{2-}) that is attributed to the dissolution of atmospheric CO_2 into
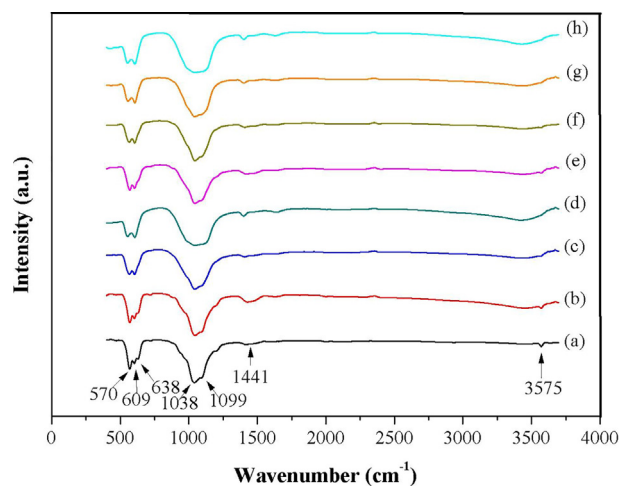

Fig. 4. FT-IR spectra of samples: (a) HAp-nUS, (b) HAp-US (c) 1.0Ce/HAp-nUS (d) 2.0Ce/HAp-nUS, (e) 0.5Ce/HAp-US, (f) 1.0Ce/HAp-US, (g) 1.5Ce/HAp-US and (h) 2.0Ce/HAp-US.
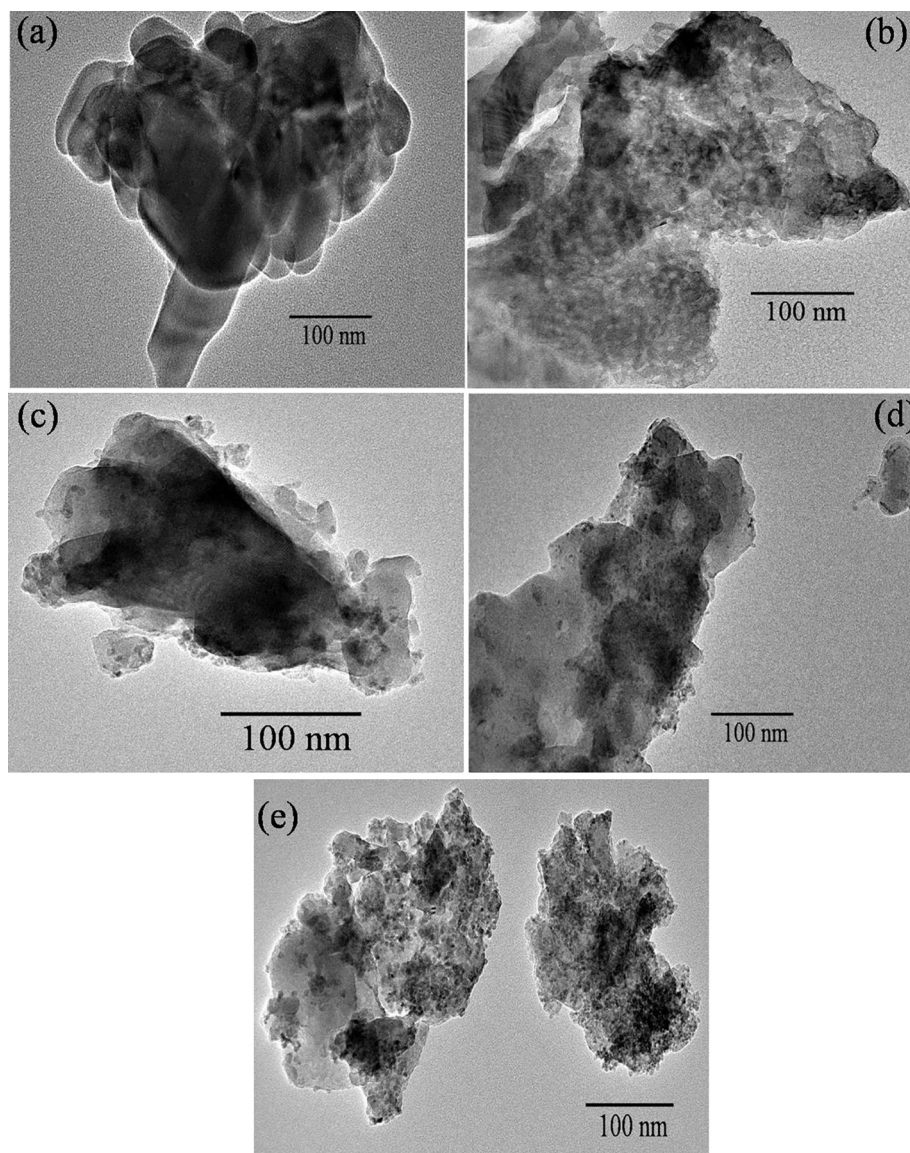
Fig. 5. TEM images of (a) HAp-nUS, (b) HAp-US, (c) 1.0Ce/HAp-US (d) 1.0Ce/HAp-US and (e) 2.0Ce/HAp-US.

the aqueous solution during synthesis. Moreover, CO_2 from air reacts with surface -OH ions of HAp-nUS and HAp-US samples to form CO_3^{2-} and water [73–75]. The peak intensity of P-O and PO_4^{3-} at 1099 and 1038 cm^{-1} was observed to diminish within the range of 1047–1090 cm^{-1} due to increasing Ce content, which causes variation and weakened bonds of PO_4^{3-} in the HAp lattice structure [72].

TEM and EDX analysis

Fig. 5 illustrates the TEM images of synthesized HAp and Ce/HAp powder samples under various Ce compositions. Based from Fig. 5(a–b), the morphology of HAp-nUS exhibits agglomeration of large, oval-shaped particles while HAp-US consists of very fine spherical particles. Ce/HAp (Fig. 5(c–e)) shows several dark spots with diameter of less than 5 nm, which could be comprised of loaded Ce species. The nanoparticles were densely distributed on the HAp surface where the density of dark spots increased with increasing Ce loading from 1.0 to 2.0%. Darker spots indicated agglomeration of HAp and Ce particles resulting from the replacement of Ca^{2+} with Ce^{4+} and Ce^{3+}. This supports the XRD result that Ce^{4+} and Ce^{3+} could be partially incorporated into the HAp structure. The morphology of HAp-US and Ce/HAp-US samples shows uniform dispersion of Ce particles onto the HAp surface, which

implies that ultrasonic radiation was effective in the synthesis of Ce/HAp. The nano-sized HAp and distribution of Ce nanoparticles could have a great impact on improving the mechanical properties of Ce/HAp materials [76].

The chemical composition of HAp and xCe/HAp was analyzed using EDX and the results are shown in Table 2. The theoretical weight percentages of Ca, P, O and Ce in all samples are found within the range of 26.58–36.0%, 15.44–17.65%, 34.55–39.47% and 6.64–23.25%, respectively. It was determined that the measured weight percentages of the elements are in the range of 21.21–29.65%, 11.59–16.24%, 38.80–45.61% and 5.34–21.49%, respectively. In general, the measured weight percentages of Ca, P and Ce have smaller values when compared to the theoretical weight percentages with the exception of O atom. It was observed that the measured oxygen weight fractions are higher than the expected values due to the atmospheric contamination by oxygen and water vapor. Moreover, the oxygen contamination caused the weight fractions of Ca, P and Ce to decrease further. Meanwhile, the percentage of Ce content increased with increasing Ce loading while the presence of carbon can be attributed to the carbon tape mounted onto SEM stub for the analysis. The EDX analysis shows the presence of Ca and P atoms where the Ca/P molar ratios of HAp-nUS and HAp-US samples were found to be 1.60 and 1.77, respectively.

Table 2
Weight and atomic percentages of Ca, P, O, Ce and C in HAp and Ce/HAp samples derived from the EDX measurements.

Samples	Ca (K)*		P (K)*		O (K)*		Ce (L)*		C (K)*	
	wt%	at%	wt%	at%	wt%	at%	wt%	at%	wt%	at%
HAp-nUS	33.58	18.15	16.24	11.36	44.59	60.39	0.00	0.00	5.60	10.10
HAp-US	33.67	17.93	14.68	10.12	44.83	59.81	0.00	0.00	6.83	12.14
1.0Ce/HAp-nUS	26.41	14.47	12.14	8.60	40.87	56.08	10.03	1.57	10.55	19.28
2.0Ce/HAp-nUS	21.21	12.64	11.59	8.94	38.88	58.02	19.75	3.36	8.57	17.04
0.5Ce/HAp-US	29.65	16.31	13.87	9.87	45.61	62.84	5.34	0.84	5.53	10.14
1.0Ce/HAp-US	28.43	16.65	13.36	10.12	43.33	63.57	10.87	1.82	4.01	7.84
1.5Ce/HAp-US	24.94	15.11	13.13	10.29	41.88	63.56	15.97	2.77	4.09	8.27
2.0Ce/HAp-US	22.49	14.36	13.09	10.82	38.80	62.08	21.49	3.93	4.13	8.80

** The shells to which electrons transition are shown for each element.

When compared with the stoichiometric HAp ratio (1.67), the higher value of Ca/P ratio of synthesized HAp-US could be attributed to the substitution of PO_4^{3-} by CO_3^{2-} whereas the lower value of HAp-nUS indicated calcium-deficient HAp [77,78]. The Ca/P molar ratios of Ce/HAp-nUS samples were observed to be 1.68 and 1.41 for 1.0Ce/HAp-nUS and 2.0Ce/HAp-nUS, respectively. Besides, the Ca/P molar ratios of Ce/HAp-US samples were found to be 1.65, 1.65, 1.47 and 1.33 for 0.5Ce/HAp, 1.0Ce/HAp, 1.5Ce/HAp and 2.0Ce/HAp, respectively. This implies that the increased deficiency in Ca^{2+} was due to the higher amount of Ce^{3+} and Ce^{4+} that could have been incorporated into the HAp lattice.

Conclusions

In the present work, nano-sized Ce/HAp particles were successfully synthesized through an ultrasonic-assisted sol-gel technique. The samples were characterized using XANES, XRD, FT-IR, TEM and EDX. In the synthesized xCe/HAp, XRD confirmed the formation of mixed phases of HAp, β-TCP and CaO. Moreover, the lattice parameters were observed to slightly increase due to the substitution of Ca^{2+} (0.106 nm) with Ce^{3+} (0.114 nm) and Ce^{4+} (0.097 nm). FT-IR measurements revealed that the partial incorporation of Ce^{3+} and Ce^{4+} into the hexagonal framework of HAp and β-TCP caused the reduced peak intensity of main functional groups such as OH^- and PO_4^{3-} groups. The morphology of pure HAp is composed of very fine spherical particles while xCe/HAp particles reveal many well-distributed dark spots with sizes less than 5 nm. Moreover, the increasing of Ce loading leads to an increase in the density of dark spots. Results of the EDX analysis illustrated that the molar ratio of Ca/P of xCe/HAp particles decreased with increasing Ce content from 0.5% to 2.0%. In general, results show that Ce^{3+} and Ce^{4+} coexisted in the crystal structure of HAp where the Ce-substituted HAp samples contained Ce^{3+} within the range of 17–18%.

Acknowledgements

Appendix A. Supplementary data

Supplementary data associated with this article can be found, in the online version, at https://doi.org/10.1016/j.rinp.2018.08.012.

References

[1] Palmer LC, Newcomb CJ, Kaltz SR, Spoerke ED, Stupp SI. Biomimetic systems for hydroxyapatite mineralization inspired by bone and enamel. Chem Rev 2008;108:4754–83. https://doi.org/10.1021/cr8004422.

[2] Dorozhkin SV. Calcium orthophosphates. J Mater Sci 2007;42:1061–95. https://doi.org/10.1007/s10853-006-1467-8.

[3] Dorozhkin SV. Bioceramics of calcium orthophosphates. Biomaterials 2010;31:1465–85. https://doi.org/10.1016/j.biomaterials.2009.11.050.

[4] Simon V, Lazăr D, Turcu RVF, Mocuta H, Magyari K, Prinz M, Neumann M, Simon S. Atomic environment in sol-gel derived nanocrystalline hydroxyapatite. Mater Sci Eng B 2009;165:247–51. https://doi.org/10.1016/j.mseb.2009.06.010.

[5] Stanic V, Dimitrijevic S, Antic-Stankovic J, Mitric M, Jokic B, Plecas IB, Raicevic S. Synthesis, characterization and antimicrobial activity of copper and zinc-doped hydroxyapatite nanopowders. Appl Surf Sci 2010;256:6083–9. https://doi.org/10.1016/j.apsusc.2010.03.124.

[6] Bernards MT, Qin C, Jiang S. MC3T3-E1 cell adhesion to hydroxyapatite with adsorbed bone sialoprotein, bone osteopontin, and bovine serum albumin. Colloids Surf B 2008;64:236–47. https://doi.org/10.1016/j.colsurfb.2008.01.025.

[7] Suchanek WL, Shuk P, Byrappa K, Riman RE, TenHuisen KS, Janas VF. Mechanochemical-hydrothermal synthesis of carbonated apatite powders at room temperature. Biomaterials 2002;23:699–710. https://doi.org/10.1016/S0142-9612(01)00158-2.

[8] Bang LT, Ishikawa K, Othman R. Effect of silicon and heat-treatment temperature on the morphology and mechanical properties of silicon-substituted hydroxyapatite. Ceram Int 2011;37:3637–42. https://doi.org/10.1016/j.ceramint.2011.06.023.

[9] Niera IS, Kolenko YV, Lebedev OI, Tendeloo GV, Gupta HS, Guitián F, Yoshimura M. An effective morphology control of hydroxyapatite crystals via hydrothermal synthesis. Cryst Growth Des 2009;9:466–74. https://doi.org/10.1021/cg800738a.

[10] Dorozhkin SV. Calcium orthophosphates in dentistry. J Mater Sci Mater Med 2013;24:1335–63. https://doi.org/10.1007/s10856-013-4898-1.

[11] Hench LL. Bioceramics. J Am Ceram Soc 1998;81:1705–28. https://doi.org/10.1111/j.1151-2916.1998.tb02540.x.

[12] Quatela VC, Chow J. Synthetic facial implants. Facial Plast Surg Clin North Am 2008;16:1–10. https://doi.org/10.1016/j.fsc.2007.09.002.

[13] Gopi D, Kanimozhi K, Bhuvaneshwari N, Indira J, Kavitha L. Novel banana peel pectin mediated green route for the synthesis of hydroxyapatite nanoparticles and their spectral characterization. Spectrochim Acta A 2014;118:589–97. https://doi.org/10.1016/j.saa.2013.09.034.

[14] Pasha R, Hill SL, Burgio DL. Evaluation of hydroxyapatite ossicular chain prostheses. Otolaryngol Head Neck Surg 2000;123:425–9. https://doi.org/10.1067/mhn.2000.109369.

[15] Fathi MH, Hanifi A. Evaluation and characterization of nanostructure hydroxyapatite powder prepared by simple sol-gel method. Mater Lett 2007;61:3978–83. https://doi.org/10.1016/j.matlet.2007.01.028.

[16] Nagai M, Nichino T. Surface conduction of porous hydroxyapatite ceramics at elevated temperatures. Sol St Ionics 1988;28–30:1456–61. https://doi.org/10.1016/0167-2738(88)90403-1.

[17] Suchanek WL, Byrappa K, Shuk P, Riman RE, Janas VF, TenHuisen KD. Mechanochemical-hydrothermal synthesis of calcium phosphate powders with coupled magnesium and carbonate substitution. J Solid State Chem 2004;177:793–9. https://doi.org/10.1016/j.jssc.2003.09.012.

[18] Wahba SMR, Darwish AS, Kamal SM. Ceria-containing uncoated and coated hydroxyapatite-based galantamine nanocomposites for formidable treatment of Alzheimer's disease in ovariectomized albino-rat model. Mat Sci Eng C 2016;65:151–63. https://doi.org/10.1016/j.msec.2016.04.041.

[19] Chahkandi M. Mechanism of Congo red adsorption on new sol-gel-derived hydroxyapatite nano-particle. Mater Chem Phys 2017;202:340–51. https://doi.org/10.1016/j.matchemphys.2017.09.047.

[20] Hirai S, Nishinaka K, Shimakage K, Uo M, Watari F. Hydroxyapatite coating on titanium substrate by the sol-gel process. J Am Ceram Soc 2004;87:29–34. https://doi.org/10.1111/j.1151-2916.2004.tb19940.x.

[21] Jones JR, Lin S, Yue S, Lee PD, Hanna JV, Smith ME, Newport RJ. Bioactive glass scaffolds for bone regeneration and their hierarchical characterization. Proc Inst Mech Eng H 2010;224:1373–87. https://doi.org/10.1243/09544119JEIM836.

[22] Brown PW. Phase relationships in the ternary system CaO-P₂O₅-H₂O at 25°C. J Am

Ceram Soc 1992;75:17–22. https://doi.org/10.1111/j.1151-2916.1992.tb05435.x.

[23] Priyadarshini B, Anjaneyulu U, Vijayalakshmi U. Preparation and characterization of sol-gel derived Ce⁴⁺ doped hydroxyapatite and its in vitro biological evaluations for orthopedic applications. Mater Des 2017;119:446–55. https://doi.org/10.1016/j.matdes.2017.01.095.

[24] Roopalakshmi S, Ravishankar R, Belaldavar S, Prasad RGSV, Phani AR. Investigation of structural and morphological characteristic of hydroxyapatite synthesized by sol-gel process. Mater Today Proc 2017;4:12026–31. https://doi.org/10.1016/j.matpr.2017.09.126.

[25] Varadarajan N, Balu R, Rana D, Ramalingam M, Sampath Kumar TS. Accelerated sonochemical synthesis of calcium deficient hydroxyapatite nanoparticles: structural and morphological evolution. J Biomater Tissue Eng 2014;4:295–9. https://doi.org/10.1016/j.matpr.2017.09.126.

[26] Tang CY, Uskokovic PS, Tsui CP, Veljovic DJ, Petrovic R, Janackovic DJ. Influence of microstructure and phase composition on the nanoindentation characterization of bioceramic materials based on hydroxyapatite. Ceram Int 2009;35:2171–8. https://doi.org/10.1016/j.ceramint.2008.11.028.

[27] Supova M. Substituted hydroxyapatites for biomedical applications: a review. Ceram Int 2015;41:9203–31. https://doi.org/10.1016/j.ceramint.2015.03.316.

[28] Guerra-López JR, Echeverría GA, Güida JA, Viña R, Punte G. Synthetic hydroxyapatites doped with Zn(II) studied by X-ray diffraction, infrared, Raman and thermal analysis. J Phys Chem Solids 2015;81:57–65. https://doi.org/10.1016/j.jpcs.2015.01.017.

[29] Kim TN, Feng QL, Kim JO, Wu J, Wang H, Chen GC, Cui FZ. Antimicrobial effects of metal ions (Ag⁺, Cu²⁺, Zn²⁺) in hydroxyapatite. J Mater Sci – Mater Med 1998;9:129–34. https://doi.org/10.1023/A:1008811501734.

[30] Aina V, Bergandi L, Lusvardi G, Malavasi G, Imrie FE, Gibson IR, Cerrato G, Ghigo D. Sr-containing hydroxyapatite: morphologies of HA crystals and bioactivity onosteoblasts cells. Mater Sci Eng C 2013;33:1132–42. https://doi.org/10.1016/j.msec.2012.12.005.

[31] Pietak AM, Reid JW, Stott MJ, Sayer M. Silicon substitution in the calcium phosphate bioceramics. Biomater 2007;28:4023–32. https://doi.org/10.1016/j.biomaterials.2007.05.003.

[32] Webster TJ, Ergun C, Doremus RH, Bizios R. Hydroxylapatite with substituted magnesium, zinc, cadmium and yttrium. II. Mechanisms of osteoblast adhesion. J Biomed Mater Res 2002;59:312–7. https://doi.org/10.1002/jbm.1247.

[33] Yasukawa A, Gotoh K, Tanaka H, Kandori K. Preparation and structure of calcium hydroxyapatite substituted with light rare earth ions. Colloids Surf A 2012;393:53–9. https://doi.org/10.1016/j.colsurfa.2011.10.024.

[34] Bang LT, Ramesh S, Purbolaksono J, Ching YC, Long BD, Chandran H, Othman R. Effects of silicate and carbonate substitution on the properties of hydroxyapatite prepared by aqueous co-precipitation method. Mater Des 2015;87:788–96. https://doi.org/10.1016/j.matdes.2015.08.069.

[35] Lee SS, Zhu H, Contreras EQ, Prakash A, Puppala HL, Colvin VL. High temperature decomposition of cerium precursors to form ceria nanocrystal libraries for biological applications. Chem Mater 2012;24:424–32. https://doi.org/10.1021/cm200863q.

[36] Rajeswari D, Gopi D, Ramya S, Kavitha L. Investigation of anticorrosive, antibacterial and in vitro biological properties of a sulphonated poly(etheretherketone)/strontium, cerium co-substituted hydroxyapatite composite coating developed on surface treated surgical grade stainless steel for orthopedic applications. RSC Adv 2014;4:61525–36. https://doi.org/10.1039/C4RA12207K.

[37] Sahu T, Bisht SS, Ranjan Das K, Kerkar S. Nanoceria: synthesis and biomedical applications. Curr Nanosci 2013;9:588–93. https://doi.org/10.2174/15734137113099990084.

[38] Yingguang L, Zhuoru Y, Jiang C. Preparation, characterization and antibacterial property of cerium substituted hydroxyapatite nanoparticles. J Rare Earths 2007;25:452–6. https://doi.org/10.1016/S1002-0721(07)60455-4.

[39] Yuntao W, Guohao R, Dongzhou D, Fan Y, Shangke P. Study on the cerium oxidation state in a Lu₀.₈Sc₀.₂BO₃ host. J Mater Chem 2011;21:17805–9. https://doi.org/10.1039/C1JM14251H.

[40] Ouyang Y, Yushan X, Shaozao T, Qingshan S, Yiben C. Structure and antibacterial activity of Ce³⁺ exchanged montmorillonites. J Rare Earths 2009;27:858–63. https://doi.org/10.1016/S1002-0721(08)60350-6.

[41] Feng Z, Liao Y, Ye M. Synthesis and structure of cerium-substituted hydroxyapatite. J. Mater Sci Mater Med 2005;16:417–21. https://doi.org/10.1007/s10856-005-6981-8.

[42] Kanchana P, Navaneethan M, Sekar C. Fabrication of Ce doped hydroxyapatite nanoparticles based on non-enzymatic electrochemical sensor for the simultaneous determination of norepinephrine, uric acid and tyrosine. Mat Sci Eng B 2017;226:132–40. https://doi.org/10.1016/j.mseb.2017.09.015.

[43] Kaygili O, Dorozhkin SV, Keser S. Synthesis and characterization of Ce-substituted hydroxyapatite by sol-gel method. Mat Sci Eng C 2014;42:78–82. https://doi.org/10.1016/j.msec.2014.05.024.

[44] Gopi D, Ramya S, Rajeswari D, Karthikeyan P, Kavitha L. Strontium, cerium co-substituted hydroxyapatite nanoparticles: Synthesis, characterization, antibacterial activity towards prokaryotic strains and *in vitro* studies. Colloids Surf A 2014;451:172–80. https://doi.org/10.1016/j.colsurfa.2014.03.035.

[45] Yuan Q, Qin C, Wu J, Xu A, Zhang Z, Liao J, Lin S, Ren X, Zhang P. Synthesis and characterization of Cerium-doped hydroxyapatite/polylactic acid composite coatings on metal substrates. Mater Chem Phys 2016;182:365–71. https://doi.org/10.1016/j.matchemphys.2016.07.044.

[46] Kurtjak M, Vukomanovic M, Suvorov D. Antibacterial nanocomposite of functionalized nanogold and gallium-doped hydroxyapatite. Mater Lett 2017;193:126–9. https://doi.org/10.1016/j.matlet.2017.01.092.

[47] Sanosh KP, Chu MC, Balakrishnan A, Kim TN, Cho SJ. Preparation and characterization of nano-hydroxyapatite powder using sol-gel technique. Bull Mater Sci 2009;32:465–70. https://doi.org/10.1007/s12034-009-0069-x.

[48] Agawane GL, Shin SW, Vanalakar SA, Suryawanshi MP, Moholkar AV, Yun JH, Gwak J, Kim JH. Synthesis of simple, low cost and benign sol-gel Cu₂ZnSnS₄ thin films: influence of different annealing atmospheres. J Mater Sci Mater Electron 2015;26:1900–7. https://doi.org/10.1007/s10854-014-2627-2.

[49] Asri RIM, Harun WSW, Hassan MA, Ghani SAC, Buyong Z. A review of hydroxyapatite-based coating techniques: Sol-gel and electrochemical depositions on biocompatible metals. J Mech Behav Biomed Mater 2016;57:95–108. https://doi.org/10.1016/j.jmbbm.2015.11.031.

[50] Kaygili O, Keser S, Ates T, Al-Ghamdi AA, Yakuphanoglu F. Controlling of dielectrical and optical properties of hydroxyapatite based bioceramics by Cd content. Powder Technol 2013;245:1–6. https://doi.org/10.1016/j.powtec.2013.04.012.

[51] Li Z, Zhang X, Hu D. Tunable fluids and green chemical processes. Chem Bull 2003;5:323–6.

[52] Stoica TF, Morosanu C, Slav A, Stoica T, Osiceanu P, Anastasescu C, Gartner M, Zaharescu M. Hydroxyapatite films obtained by sol-gel and sputtering. Thin Solid Films 2008;516:8112–6. https://doi.org/10.1016/j.tsf.2008.04.071.

[53] Kim W, Saito F. Sonochemical synthesis of hydroxyapatite from H₃PO₄ solution with Ca(OH)₂. Ultrason Sonochem 2001;8:85–8. https://doi.org/10.1016/S1350-4177(00)00034-1.

[54] Mehta D, Mondal P, Saharan VK, George S. Synthesis of hydroxyapatite nanorods for application in water defluoridation and optimization of process variables: Advantage of ultrasonication with precipitation method over conventional method. Ultrason Sonochem 2017;37:56–70. https://doi.org/10.1016/j.ultsonch.2016.12.035.

[55] Rouhani P, Taghavinia N, Rouhani S. Rapid growth of hydroxyapatite nanoparticles using ultrasonic irradiation. Ultrason Sonochem 2010;17:853–6. https://doi.org/10.1016/j.ultsonch.2010.01.010.

[56] Söhnel O, Mullin JW. Interpretation of crystallization induction periods. J Colloid Interface Sci 1998;123:43–50. https://doi.org/10.1016/0021-9797(88)90219-6.

[57] Utara S, Klinkaewnarong J. Sonochemical synthesis of nano-hydroxyapatite using natural rubber latex as a templating agent. Ceram Int 2015;41:14860–7. https://doi.org/10.1016/j.ceramint.2015.08.018.

[58] Kumar PA, Jeong YE, Gautam S, Ha HP, Lee KL, Chae KH. XANES and DRIFTS study of sulfated Sb/V/Ce/TiO₂ catalysts for NH₃-SCR. Chem Eng J 2015;275:142–51. https://doi.org/10.1016/j.cej.2015.03.124.

[59] Wu TS, Zhou Y, Sabirianov RF, Mei WN, Soo YL, Cheung CL. X-ray absorption study of ceria nanorods promoting the disproportionation of hydrogen peroxide. Chem Commun 2016;52:5003–6. https://doi.org/10.1039/C5CC10643E.

[60] Zimicz MG, Larrondo SA, Prado RJ, Lamas DG. Time-resolved in situ XANES study of the redox properties of Ce₀.₉Zr₀.₁O₂ mixed oxides. . Int J Hydrogen Energy 2012;37:14881–6. https://doi.org/10.1016/j.ijhydene.2012.01.162.

[61] de Carolis S, Pascual JL, Pettersson LGM, Baudin M, Wójcik M, Hermansson K, Palmqvist AEC, Muhammed M. Structure and electronic properties of Ca-doped CeO₂ and implications on catalytic activity: an experimental and theoretical study. J Phys Chem B 1999;103:7627–36. https://doi.org/10.1021/jp983323e.

[62] Ciobanu G, Bargan AM, Luca C. New cerium(IV)-substituted hydroxyapatite nanoparticles: Preparation and characterization. Ceram Int 2015;41:12192–201. https://doi.org/10.1016/j.ceramint.2015.06.040.

[63] Della Mea GB, Matte LP, Thill AS, Lobato FO, Benvenutti EV, Arenas LT, Jürgensen A, Hergenröder R, Poletto F, Bernardi F. Tuning the oxygen vacancy population of cerium oxide (CeO₂₋ₓ,0 < x < 0.5) nanoparticles. Appl Surf Sci 2017;422:1102–12. https://doi.org/10.1016/j.apsusc.2017.06.101.

[64] Li J, Song Z, Ning P, Zhang Q, Liu X, Li H, Huang Z. Influence of calcination temperature on selective catalytic reduction of NOₓ with NH₃ over CeO₂-ZrO₂-WO₃ catalyst. J Rare Earths 2015;33:726–35. https://doi.org/10.1016/S1002-0721(14)60477-4.

[65] Zhang P, Lu H, Zhou Y, Zhang L, Wu Z, Yang S, Shi H, Zhu Q, Chen Y, Dai S. Mesoporous MnCeOx solid solutions for low temperature and selective oxidation of hydrocarbons. Nat Commun 2015;6:1–10. https://doi.org/10.1038/ncomms9446.

[66] Kulanthaivel S, Roy B, Agarwal T, Giri S, Pramanik K, Pal K, Ray SS, Maiti TK, Banerjee I. Cobalt doped proangiogenic hydroxyapatite for bone tissue engineering application. Mater Sci Eng C 2016;58:648–58. https://doi.org/10.1016/j.msec.2015.08.052.

[67] Ellis DE, Terra J, Warschkow O, Jiang M, González GB, Okasinski JS, Bedzyk MJ, Rossi AM, Eon JG. A theoretical and experimental study of lead substitution in calcium hydroxyapatite. Phys Chem Chem Phys 2006;8:967–76. https://doi.org/10.1039/b509254j.

[68] Getman EI, Ignatov AV, Loboda SN, Abdul Jabar MAB, Zhegailo AO, Gluhova AS. Substitution of samarium for strontium on the structure of hydroxyapatite. Funct Mater 2011;18:293–7.

[69] Rameshbabu N, Sampath Kumar TS, Prabhakar TG, Sastry VS, Murty KVGK, Prasad Rao K. Antibacterial nanosized silver substituted hydroxyapatite: synthesis and characterization. J Biomed Mater Res A 2007;80:581–91. https://doi.org/10.1002/jbm.a.30958.

[70] Vijayalakshmi U, Rajeswari S. Preparation and characterization of microcrystalline hydroxyapatite using sol-gel method. Trends Biomater Artif Organs 2006;19:57–62.

[71] Tkalčec E, Popović J, Orlić S, Milardović S, Ivanković H. Hydrothermal synthesis and thermal evolution of carbonate-fluorhydroxyapatite scaffold from cuttlefish bones. Mater Sci Eng C Mater Biol Appl 2014;42:578–86. https://doi.org/10.1016/j.msec.2014.05.079.

[72] Serret A, Cabañas MV, Vallet-Regi M. Stabilization of calcium oxyapatites with lanthanum (III)-created anionic vacancies. Chem Mater 2000;12:3836–41. https://doi.org/10.1021/cm001117p.

[73] Cheng ZH, Yasukawa A, Kandori K, Ishikawa T. FTIR study of adsorption of CO₂ on

nonstoichiometric calcium hydroxyapatite. Langmuir 1998;14:6681–6. https://doi.org/10.1021/la980339n.

[74] Cheng ZH, Yasukawa A, Kandori K, Ishikawa T. FTIR study on incorporation of CO_2 into calcium hydroxyapatite. J Chem Soc Faraday Trans 1998;94:1501–5. https://doi.org/10.1039/A708581H.

[75] Waheed S, Sultan M, Jamil T, Hussain T. Comparative analysis of hydroxyapatite synthesized by sol-gel, ultrasonication and microwave assisted technique. Mater Today: Proc 2015;2:5477–84. https://doi.org/10.1016/j.matpr.2015.11.073.

[76] Mishra VK, Bhattacharjee BN, Parkash O, Kumar D, Rai SB. Mg-doped hydroxyapatite nanoplates for biomedical applications: A surfactant assisted microwave synthesis and spectroscopic investigations. J Alloy Compd 2014;614:283–8. https://doi.org/10.1016/j.jallcom.2014.06.082.

[77] Goloshchapov DL, Minakov DA, Domashevskaya EP, Seredin PV. Excitation of luminescence of the nanoporous bioactive nanocrystalline carbonate-substituted hydroxyapatite for early tooth disease detection. Results Phys 2017;7:3853–8. https://doi.org/10.1016/j.rinp.2017.09.055.

[78] Seredin PV, Goloshchapov DL, Prutskij T, Ippolitov YuA. Fabrication and characterisation of composites materials similar optically and in composition to native dental tissues. Results Phys 2017;7:1086–94. https://doi.org/10.1016/j.rinp.2017.02.025.